Research Square

Preprints are preliminary reports that have not undergone peer review.
They should not be considered conclusive, used to inform clinical practice,
or referenced by the media as validated information.

Experimental and Numerical Investigation on the Three-Dimensional Equivalent Elastic Constants and Progressive Damage of Thick-Section Composite Laminates

Yuanjie Hu
Nanjing University of Aeronautics and Astronautics
Jiaheng Liu
Nanjing University of Aeronautics and Astronautics
Shuhua Zhu
zhushuhua@nuaa.edu.cn
Nanjing University of Aeronautics and Astronautics
Yuequan Wang
Nanjing University of Aeronautics and Astronautics
Mingbo Tong
Nanjing University of Aeronautics and Astronautics
Zhijin Wang
Nanjing University of Aeronautics and Astronautics

Research Article

Keywords: Composite materials, Thick laminates, 3D equivalent elastic constants, Damage mechanics, Finite element analysis (FEA)

Posted Date: June 8th, 2026

DOI: https://doi.org/10.21203/rs.3.rs-9670246/v1

License: This work is licensed under a Creative Commons Attribution 4.0 International License.
Read Full License

Additional Declarations: No competing interests reported.

Experimental and Numerical Investigation on the Three-Dimensional Equivalent Elastic Constants and Progressive Damage of Thick-Section Composite Laminates

Yuanjie Hu[1], Jiaheng Liu[1], Shuhua Zhu[1*], Yuequan Wang[1], Mingbo Tong[1], Zhijin Wang[1]

(1. College of Aerospace Engineering, Nanjing University of Aeronautics and Astronautics, Nanjing, 210016, China)

*Corresponding author. Tel.: +86 (0)25 84896671.E-mail address: zhushuhua@nuaa.edu.cn

Abstract： Thick-section composite laminates are increasingly integrated into primary aerospace structures, yet their mechanical characterization remains a significant challenge due to complex three-dimensional (3D) stress states and high computational costs. This study presents a comprehensive integrated framework for the mechanical analysis and failure prediction of thick-section T800/PEEK laminates. First, a 3D homogenization theory was employed to derive the effective equivalent elastic constants of the periodic sub-laminates, providing a computationally efficient alternative to fully discrete models. Uniaxial tensile and compressive tests, supported by full-field DIC measurements, were conducted to validate the linear-elastic response. Subsequently, a high-fidelity 3D progressive damage model (PDM), incorporating the physically-based Puck failure criterion and a cohesive zone model, was implemented via a VUMAT subroutine in Abaqus/Explicit. The results demonstrate that the predicted macroscopic stiffness values exhibit excellent agreement with experimental data, with relative errors for all strain monitoring points constrained within 7%. Notably, the PDM achieved an exceptionally high accuracy in predicting the ultimate compressive strength, with a marginal error of only 1.23%. Microscopic observations revealed a catastrophic "brooming" failure mode driven by the synergistic interaction of delamination and out-of-plane fiber kinking. The numerical framework successfully captured the shear band localization and the degradation of lateral support, providing a robust and efficient tool for the optimal design and structural integrity assessment of thick-section composite structures.

Keywords： Composite materials; Thick laminates; 3D equivalent elastic constants; Damage mechanics; Finite element analysis (FEA)

1.Introduction

Owing to their superior specific strength, exceptional specific stiffness, excellent fatigue resistance, and highly tailorable mechanical properties, composite materials have been extensively utilized in advanced engineering sectors, particularly in the aerospace industry[1[8]. To date, aircraft featuring all-composite structural airframes have been successfully developed and deployed. Driven by continuous advancements in structural design methodologies and manufacturing technologies, the application of composite materials has progressively expanded from secondary load-bearing structures—such as landing gear doors, radomes, rudders, flaps, and ailerons—to primary load-bearing structures, including the fuselage, wings, and horizontal/vertical stabilizers[9]. This transition has inevitably led to the widespread emergence of thick-section composite laminates in modern aircraft design. For instance, the all-composite main rotor hub of the H160 helicopter exhibits a maximum thickness of 85 mm (with a minimum of 32 mm) [10]; the maximum thickness of the F-22 wing skin reaches 14.2 mm; the tail rotor flexbeam of the CH-53K heavy-lift helicopter is up to 76 mm thick; and the critical joint connections in the center wing box of the A380 airliner boast a remarkable thickness of 160 mm. It is worth emphasizing that the classification of a laminate as "thick" is not solely dictated by its nominal geometrical thickness, but is fundamentally dependent on the applied loading conditions. Particularly under compressive loading, a composite laminate with a wall thickness exceeding 4 mm is generally categorized as a thick-section structure, as the out-of-plane effects and three-dimensional stress states become significantly pronounced.

Despite the maturity of design and manufacturing technologies for thin-walled composite structures, significant technical gaps remain in the development of thick-section composite laminates. These challenges severely hinder their broader application and further advancement. To address the mechanical evaluation of composite laminates, Yildiz and Sarikanat[11] developed a finite element framework specifically tailored for the analysis of multilayered composite beams and plates. To determine the equivalent properties, they proposed a novel weighted averaging method as an alternative to the conventional arithmetic averaging approach. By evaluating various loading conditions, they systematically investigated the effects of both averaging schemes on the predictive accuracy. Comparisons with

analytical solutions demonstrated that both methods could yield satisfactory agreement under specific loading configurations. Onodera and Okabe[12] derived analytical expressions for the three-dimensional (3D) effective elastic constants of transversely isotropic laminates containing intralaminar cracks, based on continuum damage mechanics. By constructing a local stress field that satisfies the equilibrium equations, two damage parameters governing tensile and shear degradation were explicitly formulated as functions of the transverse crack density. Subsequently, employing 3D laminate theory, the effective compliance of the damaged laminate was utilized to establish an analytical steady-state cracking model. Jangravi et al.[13] proposed an equilibrium-based 3D stress recovery method by integrating higher-order shear deformation theory (HSDT) with isogeometric analysis (IGA). The employment of HSDT eliminates the reliance on shear correction factors while capturing the nonlinear transverse shear deformation, thereby enhancing the accuracy of stress predictions. Their methodology initially determines the deflection field via a Galerkin isogeometric formulation, followed by the derivation of in-plane stress gradients. Benefiting from the smooth, higher-order basis functions inherent in IGA, the out-of-plane stresses within composite laminates featuring complex anisotropic coupling could be accurately reconstructed. The accuracy and computational efficiency of this approach across various laminate configurations were rigorously validated against both analytical solutions and 3D finite element results. Jiang et al. [14] proposed a robust Lamb wave-based method for evaluating the elastic moduli of cross-ply composite plates, where the laminate was homogenized into a single-layer orthotropic continuum characterized by nine independent elastic constants. They comprehensively investigated the influence of these constants on the phase velocities of the fundamental S_0 and A_0 Lamb wave modes. The proposed methodology was computationally and experimentally validated on cross-ply carbon fiber-reinforced laminates, demonstrating excellent agreement with both theoretical predictions and conventional quasi-static tensile test data.

For thick-section composite laminates, through-thickness deformation and failure mechanisms must be explicitly accounted for. The fundamental assumption of a plane stress state is no longer valid, rendering conventional two-dimensional structural strength analysis methods inadequate for accurate predictions. To address this, Zheng et al.[15] synergistically combined experimental investigations and finite element simulations to characterize the tensile failure behaviors of thin- and thick-ply open-hole laminates. High-resolution charge-coupled device (CCD) cameras and deplying techniques were employed to capture the macroscopic failure morphologies. Concurrently, a progressive damage model coupled with a bilinear cohesive zone material (CZM) formulation was implemented in the numerical analysis to elucidate the underlying damage mechanisms. Their findings revealed distinct failure modes between the two configurations; notably, thin-ply laminates exhibited a suppressive effect on delamination. Furthermore, hole-induced delamination did not compromise the ultimate tensile strength of the open-hole laminates. Overall, thin-ply unidirectional prepreg laminates demonstrated superior strength compared to their thick-ply counterparts. Similarly focusing on hybridization, Ollic et al. [16] developed a finite element framework for unidirectional thin/thick-ply hybrid composite laminates to predict their failure modes and damage evolution under tensile loading. The incorporation of hybrid reinforcements significantly enhanced the structural ductility. The dominant damage modes—intralaminar cracking and interlaminar delamination—were accurately captured using intra- and interlaminar cohesive elements, respectively. Martinoni et al. [17] designed and fabricated unidirectional hybrid laminates with various stacking sequences, employing both experimental and numerical approaches to investigate the tensile damage modes and their propagation within thick-ply all-carbon hybrid configurations. By varying the volume fraction of thin plies, Loukil et al. [18] manufactured five distinct hybrid composite laminates and evaluated their load-bearing capacities. Their results indicated a positive correlation between the number of embedded thin plies and the overall mechanical performance of the laminates. To evaluate complex internal stress states, Bateman et al. [19] extended the deep-hole drilling technique from isotropic to orthotropic materials to assess the residual stresses within thick-section composite laminates. This technique involves drilling a small hole

perpendicular to the specimen surface, penetrating the entire thickness. The subsequent relaxation of residual stresses induces measurable diametrical deformations. By monitoring these deformations and utilizing specific calibration coefficients derived from finite element analyses, the through-thickness residual stresses of the thick composite plates could be accurately quantified. Gao et al. [20][21] conducted comprehensive experimental and numerical investigations into the thickness-dependence of the compressive properties of ultra-thick laminates. To facilitate this, they developed a heavy-duty compression testing facility and proposed a novel testing methodology tailored for ultra-thick composites. They identified delamination and fiber misalignment as the primary failure modes. Notably, as the laminate thickness increased, both the ultimate compressive strength and failure strain exhibited a gradual decline, whereas the compressive modulus remained relatively insensitive to thickness variations. In their finite element framework, the Puck failure criterion yielded the highest predictive accuracy for matrix failure-dominated specimens, with a negligible error of only 0.07% compared to experimental data. Conversely, for specimens dominated by delamination failure, the 3D Tsai-Wu failure criterion provided the most accurate strength predictions, yielding an error of 5.1%. Lee and Soutis [22] experimentally evaluated the specimen size effect on the compressive strength of unidirectional carbon fiber composite laminates. The specimens were scaled up by factors of 2 and 4 in length, width, and thickness relative to a baseline geometry. Their findings indicated a continuous degradation in compressive strength with increasing specimen size, dominated by failure modes such as fiber micro-buckling, matrix crushing, and splitting. For most specimens, particularly the thicker ones, failure prematurely initiated at the end-tab regions and the edges of the strain gauges. This premature failure was attributed to severe local stress concentrations induced by geometric discontinuities, which ultimately compromised the structural compressive strength. Similarly, Lahuerta et al. [23] examined the size effect in unidirectional glass fiber-reinforced composites under compressive loading. Scaled static and fatigue compression tests were conducted on glass/epoxy laminates with thicknesses of 4 mm, 10 mm, and 20 mm. A series of scaled specimens was meticulously designed to account for the inherent influences of manufacturing processes and final testing conditions. While static tests revealed no significant variation in the static ultimate stress across different laminate thicknesses, the fatigue tests demonstrated a distinct reduction in fatigue life, accompanied by broader confidence intervals, as the thickness increased. Niels van Hoorn et al. [24] proposed a computational framework to assess impact-induced damage in thick woven carbon fiber-reinforced polymer (CFRP) composite laminates subjected to low- and high-velocity impacts. This methodology encompassed the calibration, verification, and validation of elastic and fracture properties, alongside the determination of essential model parameters. Damage was modeled utilizing a discrete fracture approach, where cohesive interface elements were employed to capture the initiation and propagation of individual intra- and interlaminar cracks. Achieving a favorable balance between computational efficiency and prediction accuracy, this approach provides a critical tool for the optimal design and certification of thick CFRP laminates under impact loading. Max Spencer and Xiao Chen[25] experimentally studied the cracking behavior of thick carbon/glass hybrid composite laminates featuring manufacturing-induced wrinkles. Static and cyclic tensile tests on pure glass fiber and hybrid glass/carbon fiber epoxy laminates revealed that, despite possessing higher extensional stiffness, the hybrid laminates experienced premature cracking at lower stress levels compared to their pure glass counterparts. Rai et al. [26] developed a failure-mode-dependent phenomenological continuum damage model capable of coupling damage evolution across different material directions. The model parameters were rigorously calibrated using experimentally obtained stress-strain curves from uniaxial fiber tension/compression, matrix tension/compression, and in-plane/out-of-plane shear tests. Implementing load- and displacement-controlled finite element methods, they predicted the progressive damage evolution in moderately thick composite laminates under quasi-static loading conditions. When benchmarked against a failure-mode-independent damage model, the results demonstrated that the proposed model could accurately capture distinct damage modes under both tension and compression, strictly relying on fundamental material strength properties. Chen et al. [27] conducted an in-depth experimental investigation into the compressive

failure of quasi-isotropic ultra-thick carbon fiber composites, utilizing high-speed cameras coupled with digital image correlation (DIC) techniques. Uniaxial compression tests were performed on specimens with four varying thicknesses (30, 40, 50, and 60 mm) using a modified test fixture, ensuring that all macroscopic fractures occurred within the effective gauge section. Their experimental observations unveiled three distinctive compressive failure characteristics unique to ultra-thick laminates: through-thickness shear, wedge splitting, and multi-stage shear failure.

The analysis of thick-section composite laminates often encounters significant challenges regarding computational efficiency due to the prohibitive scale of high-fidelity finite element models. Furthermore, these structures exhibit pronounced transverse shear effects; coupled with the inherently low interlaminar and transverse strengths of the material, they manifest a high sensitivity to interlaminar shear failure. Consequently, classical two-dimensional laminate theories, which neglect transverse shear deformations, are inadequate for the precise analysis and optimization of thick-section configurations.

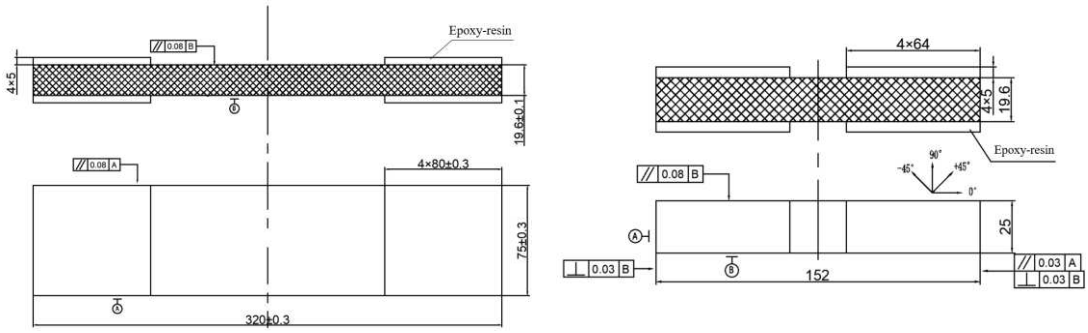
To address these limitations, this study systematically evaluates the predictive accuracy of a methodology based on the three-dimensional (3D) equivalent elasticity constants theory, integrating experimental investigations with numerical simulations. Uniaxial tensile and compressive tests were conducted on thick-section laminates, supported by full-field measurements using DIC. Corresponding numerical models were established and rigorously validated against experimental data, confirming the robustness of the equivalent elastic approach under complex loading states and providing a computationally efficient framework for the optimal design of thick laminates.

Considering the significant 3D stress states inherent in thick-section structures—specifically the through-thickness normal and shear stress components that critically threaten structural integrity—a 3D failure criterion was employed to characterize the strength and failure modes. This criterion, coupled with a progressive damage stiffness degradation model, was implemented via a user-defined material subroutine (Abaqus/VUMAT). The predicted failure loads and damage morphologies exhibited excellent agreement with experimental observations, demonstrating the reliability of the proposed finite element framework in capturing the mechanical response and failure characteristics of thick-section composite materials.

2. Materials and Experimental Methods

2.1 Specimens

To systematically investigate the macroscopic mechanical behavior of thick-section composite structures, uniaxial tensile and compressive tests were conducted. The schematic geometries and detailed dimensions of the corresponding test specimens are illustrated in Fig. 1(a) and 1(b), respectively. The composite laminates were fabricated using high-performance T800/PEEK woven fabric prepregs. To ensure optimal consolidation and achieve the desired degree of crystallinity in the thermoplastic matrix, the laminates were manufactured utilizing a hot-press molding technique. The specific processing cycle was conducted as follows: the manually laid-up prepreg stack was placed within a metallic mold and heated to a processing temperature of 385 °C at a steady heating rate of 3 °C/min. Subsequently, a constant consolidation pressure of 1.5 MPa was applied and maintained for a dwell time of 30 minutes. This isothermal holding phase facilitated complete polymer melting, proper resin flow, and the suppression of internal voids. Finally, while maintaining the applied pressure, the mold was cooled to room temperature at a strictly controlled cooling rate of 2 °C/min to induce an optimal semi-crystalline morphology. Upon consolidation, the nominal thickness of a single cured ply was 0.28 mm. The thick-section laminates comprise a total of 70 plies, resulting in an overall structural thickness of 19.6 mm. The global stacking sequence was constructed by repeating a fundamental 10-ply sub-laminate [0/36/72/-72/-36/-36/-72/72/36/0] seven times. The fundamental orthotropic mechanical properties of the T800/PEEK lamina are summarized in Table 1.



(a) tensile specimen (b) compressive specimen

Fig. 1. Schematic illustrations and detailed geometric dimensions of the thick-section laminate specimens

Table 1. Mechanical properties of laminate in present research

Property	Value
Longitudinal modulus, E_1 [MPa]	74100
Transverse modulus, E_2 [MPa]	72000
Transverse modulus, E_3 [MPa]	8330
Poisson's ratio, ν_{12}	0.07
Poisson's ratio, $\nu_{13}=\nu_{23}$	0.32
Shear modulus, G_{12} [MPa]	5450
Shear modulus, G_{13} [MPa]	4710
Shear modulus, G_{23} [MPa]	4710
Longitudinal tensile strength, X_T [MPa]	961
Longitudinal compressive strength, X_C [MPa]	724
Transverse tensile strength, Y_T [MPa]	726
Transverse tensile strength, Z_T [MPa]	62
Transverse compressive strength, Y_C [MPa]	632
Transverse compressive strength, Z_C [MPa]	180
Shear strength, S_{12} [MPa]	148
Shear strength, $S_{13}=S_{23}$ [MPa]	156

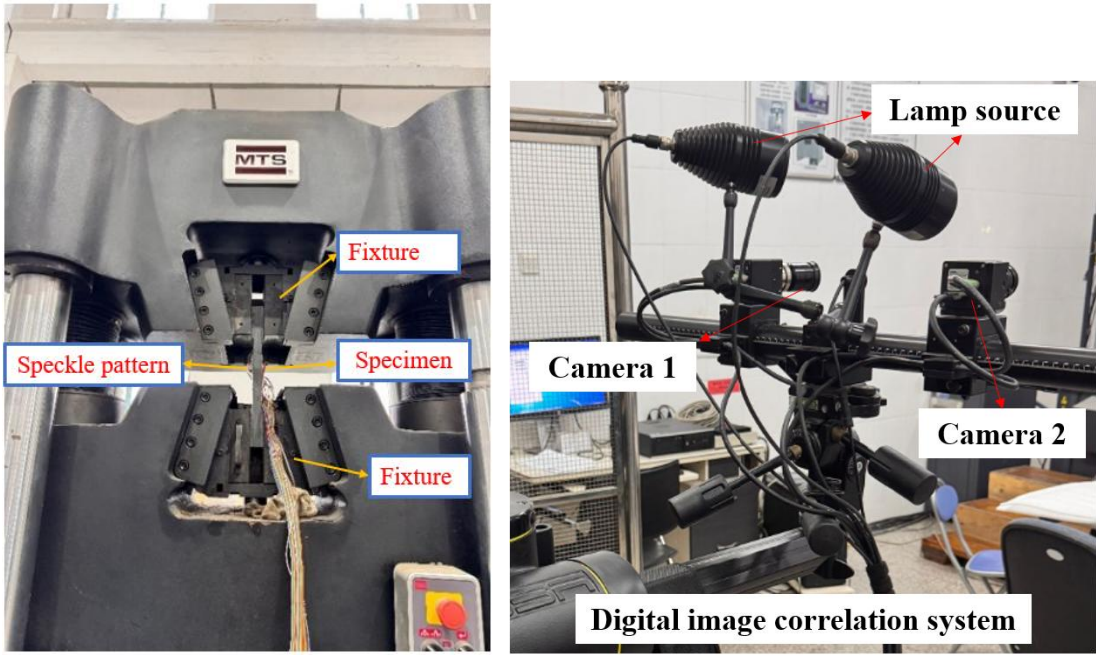
2.2 Tensile testing

To characterize the macroscopic load-strain response of the thick-section composite laminates under tensile loading, uniaxial tensile tests were conducted in strict accordance with the ASTM D3039 standard [28]. The quasi-static tests were performed utilizing an MTS E64.206 electro-hydraulic servo universal testing machine, which boasts a maximum load capacity of 2000 kN and a precision class of 0.5. To achieve comprehensive and precise deformation monitoring, the experimental setup seamlessly integrated the non-contact DIC technique with conventional electrical resistance strain gauges, as depicted in Fig. 2(a) and 2(b).

During the specimen preparation phase, the two opposite surfaces within the effective gauge section were distinctively instrumented. One surface was equipped with five strain gauges to extract localized strain data at critical locations; the specific arrangement and geometric coordinates of these gauges are illustrated in Fig. 3. The opposite surface was prepared with a stochastic speckle pattern to facilitate full-field strain analysis via the DIC system. This high-contrast pattern was generated by initially applying a uniform layer of matte white paint as the background, followed by randomly distributed droplets of matte black paint after the base coat had sufficiently dried, ensuring optimal quality for the DIC correlation algorithms.

During the testing procedure, the extremities of the specimen were rigidly clamped by the hydraulic grips of

the testing machine. The optical axes of the binocular DIC cameras were aligned perpendicularly to the speckled surface. A cold white light source was employed to provide uniform illumination, effectively mitigating any potential thermal-induced deformation of the specimen and minimizing ambient lighting fluctuations. The tests were executed under a displacement-controlled mode with a constant crosshead speed of 0.5 mm/min. Considering the superior load-bearing capacity of the thick laminates, the maximum target tensile load was set to 600 kN. Throughout the loading history, the applied load, crosshead displacement, and strain data were synchronously acquired, with discrete strain recordings captured at predefined intervals of 50 kN until the completion of the test cycle.



（a）MTS electro-hydraulic servo universal testing machine and gripping system

（b）Setup of the DIC technique

Fig. 2. Experimental setup for the uniaxial tensile tests

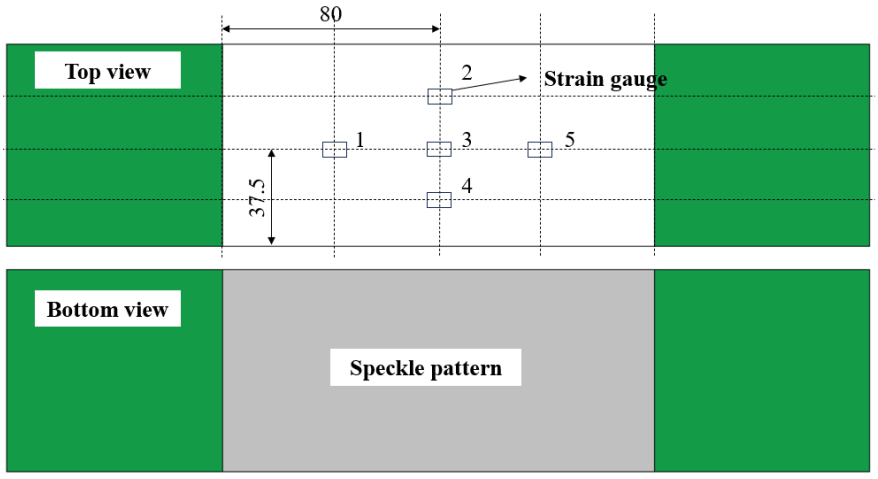


Fig. 3. Strain monitoring scheme within the effective gauge section of the tensile specimen

2.3 Compressive testing

To investigate the deformation characteristics and failure response of the thick-section laminates under compressive loading, uniaxial compression tests were conducted in accordance with the ASTM D6641 standard **Error! Reference source not found.**. The tests were performed utilizing the same MTS E64.206 electro-hydraulic

servo universal testing machine. To comprehensively capture the three-dimensional deformation of the thick composite plates during compression, a combined monitoring strategy integrating the non-contact DIC technique and conventional strain gauges was employed.

Regarding the surface instrumentation within the effective gauge section, one of the vertical observation surfaces (denoted as the 'bottom view' in Fig. 4) was prepared with a stochastic speckle pattern for DIC full-field strain analysis. To monitor the strain response on the unexposed surfaces and to meticulously detect any potential out-of-plane bending or macroscopic buckling during compression, electrical resistance strain gauges were centrally affixed to the opposite face (top view) as well as the two lateral through-thickness faces (front and rear views). The detailed strain monitoring layout and the experimental fixture assembly are illustrated in Fig. 4 and Fig. 5, respectively. The compressive tests were executed under a quasi-static displacement-controlled mode with a constant crosshead speed of 0.5 mm/min. Throughout the loading history, the applied load, crosshead displacement, and multiaxial strain data were synchronously acquired, with discrete strain recordings captured at intervals of 50 kN until the ultimate catastrophic failure of the specimens.

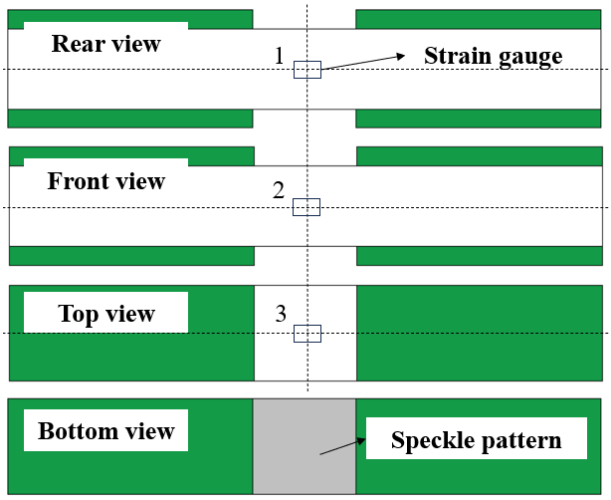


Fig. 4. Strain monitoring scheme for the compressive specimen

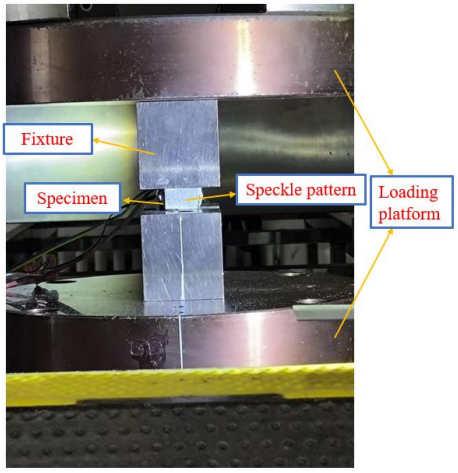


Fig. 5. Experimental setup and fixture assembly for the uniaxial compression test

3. Theory of 3D Equivalent Elastic Constants

Classical Laminate Theory (CLT) provides an effective and reliable methodology for computing the in-plane engineering constants of thin composite laminates for finite element analysis. However, constrained by the plane stress assumption, CLT is strictly applicable to two-dimensional in-plane properties and is intrinsically incapable of capturing 3D through-thickness characteristics. To overcome this limitation, this study employs the 3D equivalent constant method proposed by Sun et al. [30] to accurately derive the effective 3D elastic constants of thick woven composite laminates.

To mitigate curing-induced residual stresses and subsequent structural warpage during the manufacturing process, thick-section composite laminates in engineering applications typically adopt periodic stacking sequences. In such configurations, the sub-laminate within each period exhibits a balanced and symmetric layout. If the thickness of a single periodic sub-laminate is sufficiently small relative to the global macro-deformation of the laminate, the material can be treated using homogenization and continuum mechanics approaches, effectively neglecting its through-thickness heterogeneity. Consequently, the original discrete thick laminate can be modeled as a homogeneous 3D anisotropic solid continuum possessing equivalent global properties. Consider a periodically stacked thick composite laminate comprising a total of M individual plies. The structural block corresponding to one

periodic sequence is defined as a sub-laminate, which serves as the characteristic unit cell. Each sub-laminate consists of *N* individual plies with arbitrary fiber orientation angles; the geometrical mapping between the global laminate and the sub-laminate is schematically illustrated in Fig. 6.

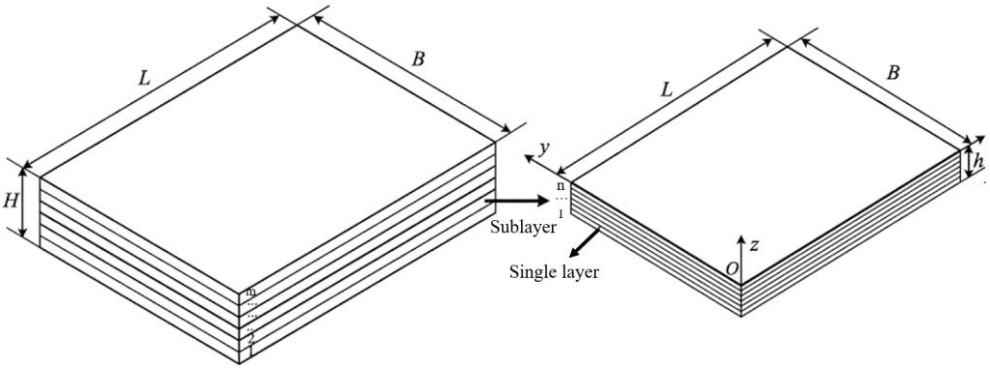


Fig. 6. Schematic representation of the geometric mapping and periodic sub-laminate structure within the thick-section composite laminate

Given the relatively minimal thickness of the unit cell, the macroscopic stresses and strains within the sub-laminate conform to the constant stress and constant strain assumptions. Furthermore, the in-plane (x-y plane) stress and strain distributions within each constituent ply of the unit cell are assumed to be uniform. Thus, the macroscopic mechanical responses can be formulated as volume-weighted averages of the ply-level values, as expressed in Eqs. (1)-(3).

$$\bar{\sigma_{ij}} = \sum_{k=1}^{N} \mu_k \sigma_{ij}^{(k)} \tag{1}$$

$$\bar{\varepsilon_{ij}} = \sum_{k=1}^{N} \mu_k \varepsilon_{ij}^{(k)} \tag{2}$$

$$\mu_k = \frac{t_k}{h} \tag{3}$$

where σ_{ij} and ε_{ij} denote the macroscopic stress and strain tensors of the sub-laminate, respectively; $\sigma_{ij}^{(k)}$ and $\varepsilon_{ij}^{(k)}$ represent the localized stress and strain within the k_{th} ply; μ_k is the volume fraction of the k_{th} ply; t_k is the thickness of the k_{th} ply; and h is the total thickness of the sub-laminate.

For a sub-laminate comprising n orthotropic plies, the 3D equivalent stiffness matrix [$\boldsymbol{C}$] can be rigorously derived using Eqs. (4)-(16) [30].

$$c_{11} = \sum_{k=1}^{N} \mu_k c_{11}^{(k)} + \sum_{k=2}^{N} \left(c_{13}^{(k)} - \lambda_{13}\right) \mu_k \left(c_{13}^{(1)} - c_{13}^{(k)}\right) / c_{33}^{(k)} \tag{4}$$

$$c_{12} = \sum_{k=1}^{N} \mu_k c_{12}^{(k)} + \sum_{k=2}^{N} \left(c_{13}^{(k)} - \lambda_{13}\right) \mu_k \left(c_{23}^{(1)} - c_{23}^{(k)}\right) / c_{33}^{(k)} \tag{5}$$

$$c_{13} = \sum_{k=1}^{N} \mu_k c_{13}^{(k)} + \sum_{k=2}^{N} \left(c_{33}^{(k)} - \lambda_{33}\right) \mu_k \left(c_{13}^{(1)} - c_{13}^{(k)}\right) / c_{33}^{(k)} \tag{6}$$

$$c_{22} = \sum_{k=1}^{N} \mu_k c_{22}^{(k)} + \sum_{k=2}^{N} \left(c_{23}^{(k)} - \lambda_{23}\right) \mu_k \left(c_{23}^{(1)} - c_{23}^{(k)}\right) / c_{33}^{(k)} \tag{7}$$

$$c_{23} = \sum_{k=1}^{N} \mu_k c_{23}^{(k)} + \sum_{k=2}^{N} \left(c_{33}^{(k)} - \lambda_{33}\right) \mu_k \left(c_{23}^{(1)} - c_{23}^{(k)}\right) / c_{33}^{(k)} \tag{8}$$

$$c_{33} = 1 / \left(\sum_{k=1}^{N} \mu_k / c_{33}^{(k)} \right) \tag{9}$$

$$c_{16} = \sum_{k=1}^{N} \mu_k c_{16}^{(k)} + \sum_{k=2}^{N} \left(c_{13}^{(k)} - \lambda_{13} \right) \mu_k \left(c_{36}^{(1)} - c_{36}^{(k)} \right) / c_{33}^{(k)} \tag{10}$$

$$c_{26} = \sum_{k=1}^{N} \mu_k c_{26}^{(k)} + \sum_{k=2}^{N} \left(c_{23}^{(k)} - \lambda_{23} \right) \mu_k \left(c_{36}^{(1)} - c_{36}^{(k)} \right) / c_{33}^{(k)} \tag{11}$$

$$c_{36} = \sum_{k=1}^{N} \mu_k c_{36}^{(k)} + \sum_{k=2}^{N} \left(c_{33}^{(k)} - \lambda_{33} \right) \mu_k \left(c_{36}^{(1)} - c_{36}^{(k)} \right) / c_{33}^{(k)} \tag{12}$$

$$c_{66} = \sum_{k=1}^{N} \mu_k c_{66}^{(k)} + \sum_{k=2}^{N} \left(c_{36}^{(k)} - \lambda_{36} \right) \mu_k \left(c_{36}^{(1)} - c_{36}^{(k)} \right) / c_{33}^{(k)} \tag{13}$$

$$c_{44} = \left(\sum_{k=1}^{N} \mu_k c_{44}^{(k)} / \Delta_k \right) / \Delta \tag{14}$$

$$c_{45} = \left(\sum_{k=1}^{N} \mu_k c_{45}^{(k)} / \Delta_k \right) / \Delta \tag{15}$$

$$c_{55} = \left(\sum_{k=1}^{N} \mu_k c_{55}^{(k)} / \Delta_k \right) / \Delta \tag{16}$$

where,

$$\lambda_{13} = c_{13}, \quad \lambda_{23} = c_{23}, \quad \lambda_{33} = c_{33}, \quad \lambda_{36} = c_{36} \tag{17}$$

$$\Delta = \left(\sum_{k=1}^{N} \frac{\mu_k c_{44}^{(k)}}{\Delta_k} \right) \left(\sum_{k=1}^{N} \frac{\mu_k c_{55}^{(k)}}{\Delta_k} \right) - \left(\sum_{k=1}^{N} \frac{\mu_k c_{45}^{(k)}}{\Delta_k} \right)^2 \tag{18}$$

$$\Delta_k = c_{44}^{(k)} c_{55}^{(k)} - \left(c_{45}^{(k)} \right)^2 \tag{19}$$

By inverting the equivalent stiffness matrix, the effective compliance matrix [$\boldsymbol{S}$] of the typical unit cell is obtained, as given by Eq. (20).

$$\overline{S} = \overline{C}^{-1} \tag{20}$$

Based on the fundamental constitutive relationships between engineering elastic constants and compliance coefficients for 3D anisotropic continua, the 3D equivalent elastic constants of the unit cell (i.e., the sub-laminate) can be explicitly extracted, as formulated in Eq. (21).

$$\begin{cases} E_x = \dfrac{1}{s_{11}}, E_y = \dfrac{1}{s_{22}}, E_z = \dfrac{1}{s_{33}} \\ \mu_{yz} = -\dfrac{s_{23}}{s_{22}}, \mu_{zx} = -\dfrac{s_{31}}{s_{33}}, \mu_{xy} = -\dfrac{s_{21}}{s_{11}} \\ G_{yz} = \dfrac{1}{s_{44}}, G_{xz} = \dfrac{1}{s_{55}}, G_{xy} = \dfrac{1}{s_{66}} \end{cases} \tag{21}$$

Since the global thick-section laminate is constructed through the periodic repetition of this specific sub-laminate along the thickness direction, it is physically sound, under periodic boundary assumptions, to equate the effective 3D elastic constants of the sub-laminate to those of the macroscopic thick laminate. Therefore, Eq. (21) directly yields the global 3D equivalent elastic constants required for the subsequent 3D finite element structural analysis.

4. Progressive damage modeling approach

The progressive damage and ultimate failure of fiber-reinforced composite laminates result from the synergistic

interactions of multiple complex mechanisms, including fiber breakage and pull-out, matrix cracking, and interlaminar delamination. In recent years, Progressive Damage Models (PDMs) have emerged as an essential methodology for predicting the macroscopic mechanical responses and failure modes of composite laminates subjected to quasi-static loading. These models have demonstrated robust efficacy and high fidelity in previous investigations concerning the progressive failure of constituent fibers and matrices [31]. Specifically, fiber kinking has been unequivocally identified as the dominant failure mechanism in laminates subjected to longitudinal compression [32]. For unidirectional laminates, initial fiber misalignment can trigger localized fiber rotation, subsequently precipitating matrix shear yielding or catastrophic shear failure. Upon reaching a critical load threshold, localized kink bands propagate abruptly across the entire width of the specimen, followed by a stable longitudinal extension along the fiber direction. Ultimately, the severe localized bending stresses concentrated within these bands culminate in macroscopic fiber breakage.

4.1 Intralaminar damage model

The damage mechanisms inherent in composite materials are highly complex; therefore, the selection of an appropriate failure criterion is crucial for enhancing the predictive accuracy of structural strength analyses. Composite failure criteria are generally classified into two broad categories: non-failure-mode-dependent criteria (such as the Maximum Stress, Hoffman [33] , Tsai-Hill [34] , and Tsai-Wu [35] criteria) and failure-mode-dependent criteria (including the Hashin [36] , Chang-Chang [37] [38] , and Puck [39] criteria). To accurately capture the complex failure behaviors of thick-section composite laminates under triaxial stress states, this study employs the physically-based Puck failure criterion to govern the initiation and evolution of intralaminar damage. The Puck criterion postulates that matrix failure is governed by the synergistic action of the normal stress (σ_n) and two associated shear stress components (τ_{nt} and τ_{nl}) acting upon a "potential fracture plane" (also referred to as the action plane). This arbitrary plane is oriented parallel to the fiber direction, as schematically illustrated in Fig. 7, which delineates the global natural coordinate system ($x_1 - x_2 - x_3$) and the local fracture plane coordinate system ($x_l - x_n - x_t$). This criterion demonstrates exceptional robustness in capturing complex damage mechanisms within both symmetric and asymmetric laminates. Specifically, under compressive loading, it enables the precise prediction of matrix damage initiation and its subsequent propagation. Numerical analyses further facilitate the effective characterization of distinct failure modes across various stacking sequences, notably matrix cracking and fiber micro-buckling. Compared to conventional stress-based phenomenological approaches, the Puck-based model exhibits superior physical fidelity in predicting damage growth trajectories.

The damage evolution process is analytically resolved through rigorous tensor transformations between the natural coordinate system and the principal damage axis system. The effective stress components acting on the potential fracture plane are explicitly calculated using Eq. (22).

$$\begin{aligned} \sigma_n &= \sigma_2 \cos^2\theta + \sigma_3 \sin^2\theta + 2\tau_{23} \sin\theta\cos\theta \\ \tau_{nt} &= (\sigma_3 - \sigma_2)\sin\theta\cos\theta + \tau_{23}\left(\cos^2\theta - \sin^2\theta\right) \\ \tau_{nl} &= \tau_{13}\sin\theta + \tau_{12}\cos\theta \end{aligned} \tag{22}$$

Furthermore, the Puck criterion distinguishes four independent failure modes within the composite lamina: fiber tension, fiber compression, matrix tension, and matrix compression. The corresponding damage initiation conditions are expressed in Eqs. (23)-(26).

Fiber tensile failure ($\sigma_1 \geqslant 0$):

$$f_{\mathrm{FF}} = \frac{\sigma_1}{R_{\parallel}^{\mathrm{t}}} \tag{23}$$

Fiber compressive failure ($\sigma_1 < 0$):

$$f_{\mathrm{FF}}=-\frac{\sigma_1}{R_{\parallel}^{\mathrm{c}}} \tag{24}$$

Matrix tensile failure ($\sigma_n \geqslant 0$):

$$f_{\mathrm{IFF}}(\theta)=\left[\left(\frac{1}{R_{\perp}^{\mathrm{t}}}-\frac{p_{\perp\psi}^{\mathrm{t}}}{R_{\perp\psi}^{\mathrm{A}}}\right)^2\sigma_n^2(\theta)+\left(\frac{\tau_{nt}(\theta)}{R_{\perp\perp}^{\mathrm{A}}}\right)^2+\left(\frac{\tau_{nl}(\theta)}{R_{\perp\parallel}}\right)^2\right]^{\frac{1}{2}}+\frac{p_{\perp\psi}^{\mathrm{t}}}{R_{\perp\psi}^{\mathrm{A}}}\sigma_n(\theta) \tag{25}$$

Matrix tensile failure ($\sigma_n < 0$):

$$f_{\mathrm{IFF}}(\theta)=\left[\left(\frac{p_{\perp\psi}^{\mathrm{c}}}{R_{\perp\psi}^{\mathrm{A}}}\sigma_n(\theta)\right)^2+\left(\frac{\tau_{nt}(\theta)}{R_{\perp\perp}^{\mathrm{A}}}\right)^2+\left(\frac{\tau_{nl}(\theta)}{R_{\perp\parallel}}\right)^2\right]^{\frac{1}{2}}+\frac{p_{\perp\psi}^{\mathrm{c}}}{R_{\perp\psi}^{\mathrm{A}}}\sigma_n(\theta) \tag{26}$$

Where, $R_{\perp\perp}^{\mathrm{A}}=\dfrac{R_{\perp}^{\mathrm{c}}}{2\left(1+p_{\perp\perp}^{c}\right)}$, $\dfrac{p_{\perp\psi}^{\mathrm{t,c}}}{R_{\perp\psi}^{\mathrm{A}}}=\dfrac{p_{\perp}^{\mathrm{t,c}}}{R_{\perp\perp}^{\mathrm{A}}}\cos^2\psi+\dfrac{p_{\perp\parallel}^{\mathrm{t,c}}}{R_{\perp\parallel}^{\mathrm{A}}}\sin^2\psi$, $\cos^2\psi=\dfrac{\tau_{nt}^2}{\tau_{nt}^2+\tau_{nl}^2}$, $\sin^2\psi=\dfrac{\tau_{nl}^2}{\tau_{nt}^2+\tau_{nl}^2}$; $R_{\parallel}^{\mathrm{t}}$ and $R_{\parallel}^{c}$ denote the tensile and compressive strengths along the fiber direction, respectively; $R_{\perp}^{\mathrm{t}}$ and $R_{\perp}^{\mathrm{c}}$ represent the tensile and compressive strengths transverse to the fibers; and $R_{\perp\parallel}$ is the in-plane matrix shear strength. $\sigma_n(\theta)$, $\tau_{nt}(\theta)$ and $\tau_{nl}(\theta)$ denote the effective stress components operating on the potential matrix fracture plane. Additionally, $p_{\perp\parallel}^{\mathrm{t}}$, $p_{\perp\perp}^{t}$, $p_{\perp\parallel}^{c}$ and $p_{\perp\perp}^{c}$ are the inclination parameters, which characterize the influence of varying normal stress states (tension vs. compression) on the slope of the fracture envelope. The recommended inclination parameters tailored for the carbon fiber composites investigated herein are detailed in Table 2.

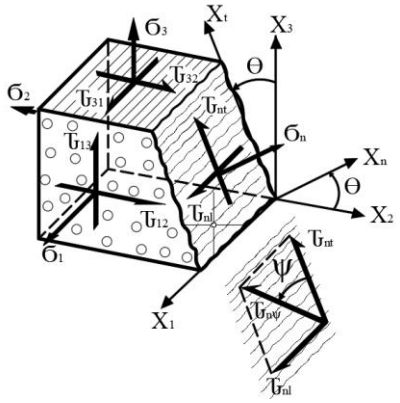


Fig. 7. Definition of the local coordinate system and stress components on the potential fracture plane

Table 2. Recommended inclination parameters of carbon fiber composites for the Puck failure criterion

$p_{\perp\parallel}^{\mathrm{t}}$	$p_{\perp\parallel}^{c}$	$p_{\perp\perp}^{t}$	$p_{\perp\perp}^{c}$
0.35	0.30	0.25-0.30	0.25-0.30

Upon satisfying any of the aforementioned damage initiation criteria, the material undergoes progressive performance degradation, characterized by a reduction in macroscopic load-bearing capacity and structural stiffness. Material stiffness degradation models are typically classified into three typologies (as depicted in Fig. 8): the constant stress model, the instantaneous degradation (sudden unloading) model, and the gradual unloading model (progressive softening). The constant stress model assumes no reduction in load-bearing capacity post-initiation, which physically contradicts actual material behavior; the instantaneous degradation model abruptly reduces the stiffness to zero or a minimal residual value, a simplistic approach heavily reliant on empirical calibration. Conversely, the progressive softening model postulates that the load-bearing capacity dissipates continuously as a function of an internal damage variable, more accurately reflecting the physical fracture process.

Consequently, this study adopts a bilinear progressive damage softening model governed by the fracture energy release rate(G_{c}). As illustrated by the trajectory $\triangle abc$ in Fig. 8, the segment *ab* represents the linear elastic regime where the damage variable remains zero; damage initiates at peak point *b*, triggering the onset of fracture energy

dissipation; as the strain increases to point *c*, the material undergoes complete structural failure, yielding a damage variable of 1. The area bounded by $\triangle abc$ is physically equivalent to the critical fracture energy density of the material. Based on energy equivalence, the equivalent strain (ε_{eq}^{f}) at complete failure can be derived via Eq. (27).

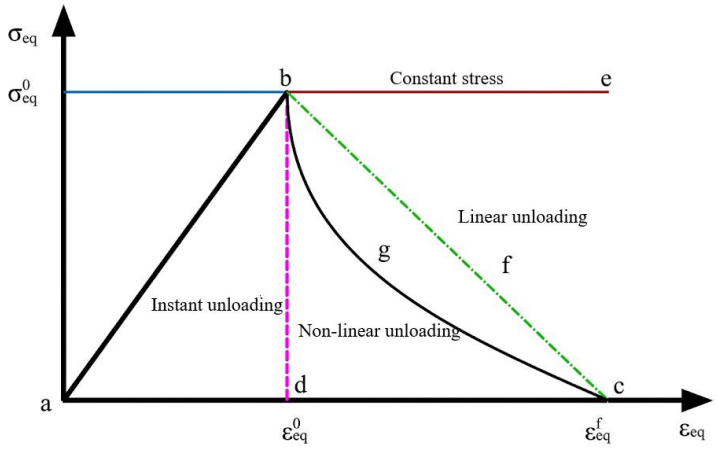


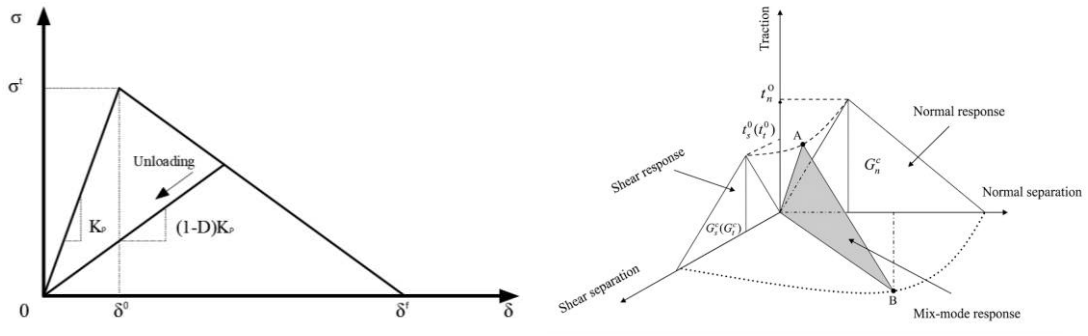
Fig. 8. Material performance degradation trajectories post-damage initiation

$$\varepsilon_{\mathrm{eq}}^{\mathrm{f}}=\frac{2G_{\mathrm{c}}}{\sigma_{\mathrm{eq}}^{0}L^{\mathrm{e}}}=\frac{2g_{\mathrm{c}}}{\sigma_{\mathrm{eq}}^{0}} \tag{27}$$

Where, σ_{eq}^{0} defines the equivalent peak stress at damage initiation, G_{c} is the critical fracture energy release rate, and g_{c} represents the energy density smeared over the characteristic length. The properties used to model the laminate are given in Table 1.

4.2 Interface damage model

Interlaminar delamination in composite materials typically initiates at the physical interfaces between plies with varying orientations, predominantly driven by severe out-of-plane stress concentrations induced by free-edge effects. Within the finite element framework, two mainstream methodologies are generally employed to simulate interfacial delamination: the Virtual Crack Closure Technique (VCCT), rooted in linear elastic fracture mechanics (LEFM), and the CZM, based on continuum damage mechanics (CDM) [40] [41]. Although VCCT is extensively utilized for crack propagation analysis, its application necessitates the pre-definition of initial flaws (pre-cracks) and presumed crack propagation trajectories, rendering it inherently incapable of predicting the natural onset of delamination. In contrast, the CZM circumvents this limitation by globally embedding cohesive interface elements between adjacent solid plies. Governed by specific constitutive laws, the progressive degradation and ultimate failure of these cohesive elements simulate interlaminar failure, thereby enabling the simultaneous prediction of both crack initiation and propagation within a unified computational framework. This study adopts the widely recognized bilinear traction-separation law to characterize the constitutive behavior of the cohesive elements. The bilinear traction-separation response under pure-mode and mixed-mode loading conditions is schematically illustrated in Fig. 9(a) and 9(b), respectively.



(a) Typical bilinear traction–separation law

(b) The cohesive zone model under mixed-mode loading

Fig. 9. 3D constitutive models for cohesive elements[40]

The onset of interfacial damage is governed by the quadratic nominal stress criterion [42], formulated as:

$$\left\{\frac{\langle t_n \rangle}{R_n}\right\}^2 + \left\{\frac{t_s}{R_s}\right\}^2 + \left\{\frac{t_t}{R_t}\right\}^2 = 1 \tag{28}$$

where t_n denotes the normal traction stress, while t_s and t_t represent the two orthogonal transverse shear tractions. The Macauley bracket, defined as $\langle x \rangle = \max(0, x)$, is deliberately employed to ensure that purely compressive normal stresses do not contribute to the initiation of interlaminar damage.

During the damage evolution phase, the Benzeggagh-Kenane (B-K) criterion, based on fracture energy dissipation, is employed to govern the propagation of delamination under mixed-mode loading scenarios [42]. Post-initiation, the cohesive elements undergo linear stiffness degradation. Complete interfacial failure occurs when the equivalent mixed-mode strain energy release rate equates to the critical threshold. The mathematical expression of the B-K criterion is presented in Eq. (29).

$$G_{IC} + (G_{IIC} - G_{IC})\left(\frac{G_{shear}}{G_T}\right)^{\eta} = G_{TC} \tag{29}$$

Where η is the material-specific B-K exponent, designated as 1.3 in this study [43]. G_{IC} and G_{IIC} denote the critical strain energy release rates (fracture toughness) for Mode I (normal tension) and Mode II (in-plane shear), respectively. G_{shear} represents the sum of the out-of-plane shear energy release rates, and G_T is the total strain energy release rate. $G_{shear} = G_{II} + G_{III}$, $G_T = G_I + G_{shear}$. The comprehensive interfacial material and fracture parameters utilized for the CZM are summarized in Table 3.

Table 3. Material parameters used in cohesive zone model

Interface parameters	Value
Modulus [GPa]	t_n=t_s=t_t
Maximum failure strength [MPa]	R_n=50; R_s=R_t=80
Critical fracture energy [J/mm2]	G_{IC}=0.6; G_{IIC}=1.12

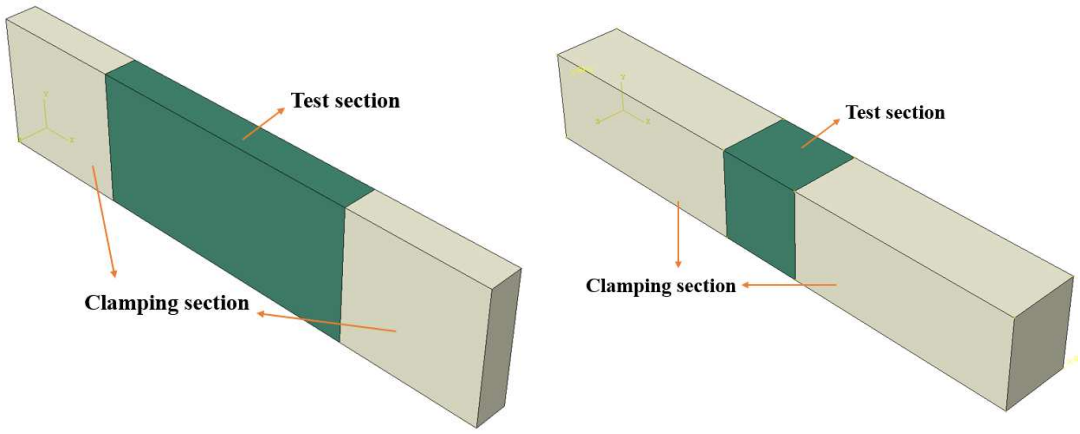
5. Numerical implementation

To comprehensively evaluate and validate the proposed theoretical framework, numerical models were developed utilizing the commercial finite element code Abaqus 2022. Initially, a macroscopic equivalent model was constructed to verify the efficacy of the homogenized stiffness parameters. Subsequently, a high-fidelity 3D progressive damage model was established based on the thick-section compression tests. The failure criteria and damage evolution methodologies described in preceding sections were coded into a user-defined material subroutine (VUMAT) to profoundly analyze the damage mechanisms and failure characteristics of thick composite laminates

under complex loading.

5.1 Geometrical details

The thick-section composite laminates consist of seven periodic sub-laminates, with a global stacking sequence of $[0/36/72/-72/-36/-36/-72/72/36/0]_7$. The nominal cured thickness of a single woven prepreg ply is 0.28 mm, resulting in a sub-laminate thickness of 2.8 mm and a total laminate thickness of 19.6 mm. To maintain strict consistency with the physical experiments, the effective gauge section dimensions of the unnotched tension model were set to 160 mm × 75 mm × 19.6 mm, whereas those of the unnotched compression model were 24 mm × 25 mm × 19.6 mm. Local material coordinate systems were explicitly defined for each ply to accurately map the principal fiber orientations and the orthotropic constitutive behaviors. The geometric models for macroscopic tension and compression are illustrated in Fig. 10(a) and 10(b), respectively.



(a) unnotched tensile specimen (b) unnotched compressive specimen

Fig. 10. Geometric solid models for the finite element analysis

5.2 Finite element model

To verify the accuracy of the 3D equivalent elastic constants, a macroscopically homogenized finite element model was established. This model was discretized into 7 elements through the thickness (element thickness of 2.8 mm), matching the number of sub-laminates, and was globally assigned the homogenized 3D equivalent elastic parameters listed in Table 4. This specific model excludes nonlinear material damage evolution and is exclusively utilized to extract the global structural stiffness and localized deformation responses during the linear elastic regime.

The boundary conditions for the tensile and compressive equivalent models are depicted in Fig. 11(a) and 11(b). To accurately simulate the actual clamping effects of the steel grips in the experiments, the gripping regions at both extremities were defined as rigid bodies. The nodal degrees of freedom on the cross-sectional faces of these regions were tied to independent reference points (RP-1 and RP-2) via kinematic coupling constraints. During the explicit solution procedure, the left reference point (RP-2) was fully encastred ($U_x=U_y=U_z=0$), while the right reference point (RP-1) was constrained in all directions except for the translational degree of freedom along the loading axis (X-direction), where a smooth step displacement loading was applied.

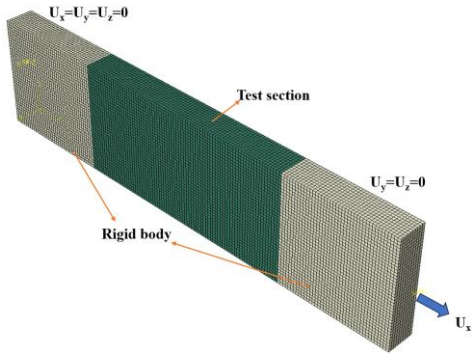
Table 4. 3D equivalent elastic parameters

Property	Value	Equivalent Elastic Constants
Longitudinal modulus, E_1 [MPa]	74100	52650
Transverse modulus, E_2 [MPa]	72000	52650
Transverse modulus, E_3 [MPa]	8330	8330
Poisson's ratio, ν_{12}	0.07	0.329

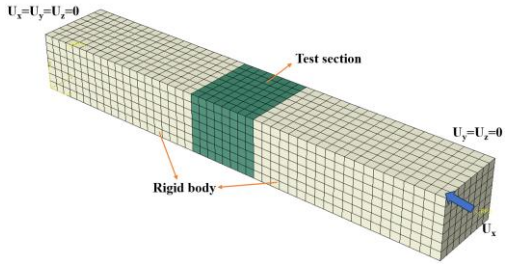
Poisson's ratio, $\nu_{13}=\nu_{23}$	0.32	0.2306
Shear modulus, G_{12} [MPa]	5450	19808
Shear modulus, G_{13} [MPa]	4710	4710
Shear modulus, G_{23} [MPa]	4710	4710

For the progressive failure analysis of the thick laminates, a highly refined ply-by-ply 3D model was constructed (Fig. 11(c)). The model explicitly incorporates 70 plies, each 0.28 mm thick. All intralaminar solid regions were discretized using eight-node hexahedral elements with reduced integration and hourglass control (C3D8R). To suppress spurious zero-energy modes (hourglassing) potentially induced by reduced integration, a stiffness-based relaxation method was rigorously applied. The in-plane mesh dimensions of the solid elements were refined to 0.343 mm × 0.357 mm, ensuring that both the in-plane aspect ratio and the through-thickness to in-plane aspect ratio remained close to unity, thereby guaranteeing high fidelity in stress field computations.

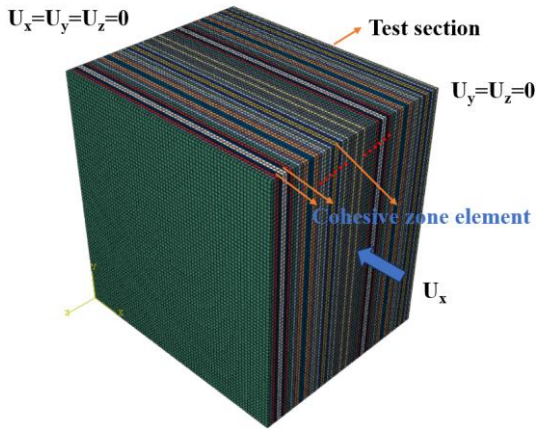
Intralaminar failure was driven by the VUMAT subroutine, which encoded the 3D Puck failure criteria and a progressive stiffness degradation model governed by fracture energy dissipation. To capture interfacial debonding and delamination propagation through the thickness, zero-thickness eight-node 3D cohesive elements (COH3D8) were globally embedded between adjacent solid plies. These cohesive elements share nodes with the adjacent solid elements to ensure absolute continuity of the displacement field in the pristine state. An element deletion mechanism was triggered to remove a solid element from the mesh once its fiber and matrix compressive damage variables concurrently reached the critical threshold of 1. The intralaminar fracture properties and interfacial cohesive parameters utilized in the finite element framework are comprehensively summarized in Table 1 and Table 3, respectively.



(a) mesh and constraints for the tensile specimen



(b) mesh and constraints for the compressive specimen



(c) ply-by-ply model for progressive failure analysis (gauge section only)

Fig. 11. Finite element computational models and boundary conditions

6. Results and discussion

6.1 Validation of 3D Equivalent Elastic Constants

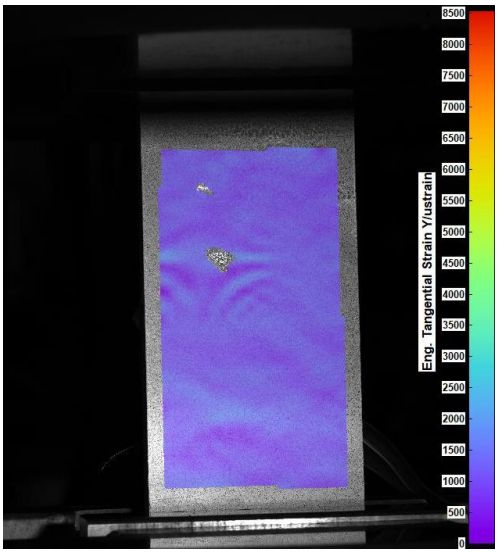
6.1.1 Tensile response and validation of macroscopic stiffness

To verify the applicability and accuracy of the 3D equivalent elastic constant theory for thick-section woven composite laminates, this section presents a comprehensive evaluation combining qualitative full-field observations and quantitative localized analyses under uniaxial tensile loading. The thick-section laminate (total thickness of 19.6 mm) comprises seven periodic sub-laminates ([0/36/72/-72/-36/-36/-72/72/36/0]), with a nominal ply thickness of 0.28 mm. The homogenized equivalent elastic parameters (summarized in Table 4) were globally assigned to the macroscopic finite element model. The numerical boundary conditions were rigorously matched to the experimental setup: the clamping regions at both extremities were constrained as rigid bodies (implemented via reference points RP-1 and RP-2), with the left end fully encastred and the right end subjected to a constant-rate tensile load.

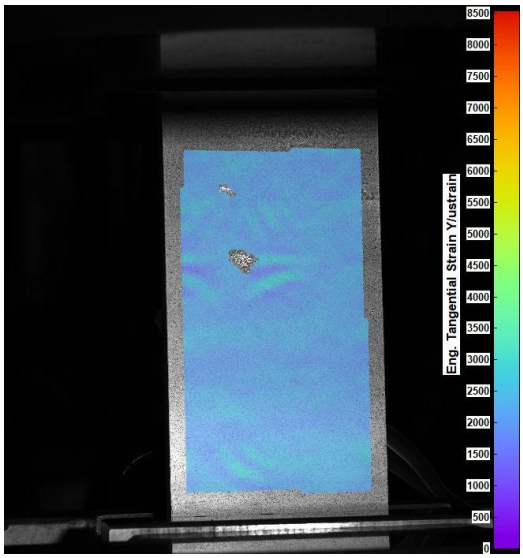
Regarding the full-field deformation characteristics, Fig. 12 illustrates the evolution of the longitudinal surface strain field for a representative specimen (RS7-WLS-1) across various load levels (ranging from 90 kN to 600 kN). The strain contour maps, acquired via the DIC technique, demonstrate that the surface strain field within the effective gauge section remains highly uniform as the applied load escalates. No pronounced localized strain concentrations or distortion phenomena were observed. This macroscopic observation visually corroborates that the thick-section laminate possesses excellent global synergistic deformation capabilities under tensile loading.

To quantitatively validate the accuracy of the equivalent model throughout the entire loading history, the experimental load-strain curves at five discrete measurement locations on the surface of the representative specimen (RS7-WLS-1) were extracted and compared against the predicted responses from corresponding nodal positions in the FEM model (Fig. 13). Given the exceptionally high repeatability and consistency in the macroscopic tensile responses across the six replicate specimens, RS7-WLS-1 was selected as the baseline for this detailed history analysis. As depicted in Fig. 13, within the entire tensile loading envelope from 0 to 600 kN, the experimental strains at all five monitoring points exhibit a strictly linear increase with respect to the applied load. No nonlinear stiffness degradation inflection points—which typically indicate material yielding or damage initiation—were detected. This confirms that the thick-section laminate maintains robust linear-elastic synergistic deformation prior to reaching the predefined target load. A comparative analysis reveals that the slopes of the FEM-predicted curves are in excellent agreement with the experimental data. Because the slope of the load-strain curve directly dictates the macroscopic structural stiffness, this high degree of consistency across the entire loading history provides compelling evidence: the derived equivalent longitudinal modulus (E_1) and associated Poisson's ratios can precisely characterize the linear-elastic constitutive response of thick-section composites under macroscopic 3D stress states.

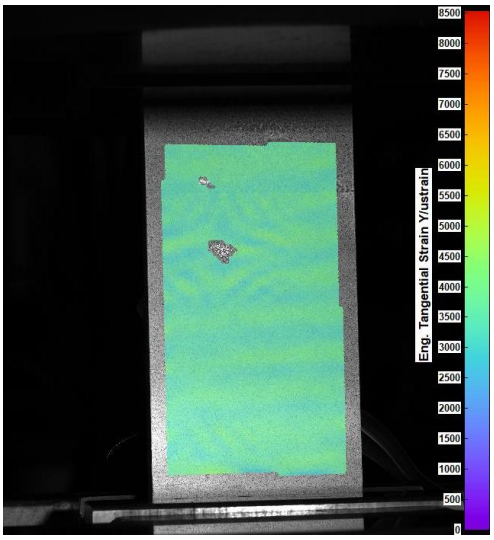
For a more rigorous statistical assessment of the numerical prediction accuracy, the localized maximum tensile strains on the specimen surfaces at the terminal load of 600 kN were extracted and compared with the finite element calculations (Table 5). The experimental results indicate that the longitudinal maximum strains across the six replicate specimens (RS7-WLS-1 to RS7-WLS-6) exhibit remarkable consistency at each respective measurement point. Comparing the average experimental values with the FEM predictions reveals that the relative errors for all five measurement locations are constrained to exceptionally low levels (e.g., the error at Strain 3 is merely 0.17%, with the maximum error being 1.67% at Strain 4). Such high-fidelity predictions not only validate the rationality of the applied numerical boundary conditions but also directly substantiate the superior accuracy and reliability of the proposed 3D equivalent elastic constant framework in predicting the macroscopic tensile stiffness of thick-section woven composite laminates.



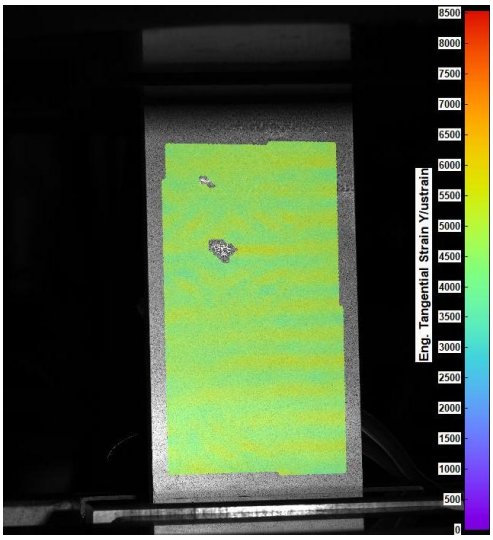
(a) 90KN



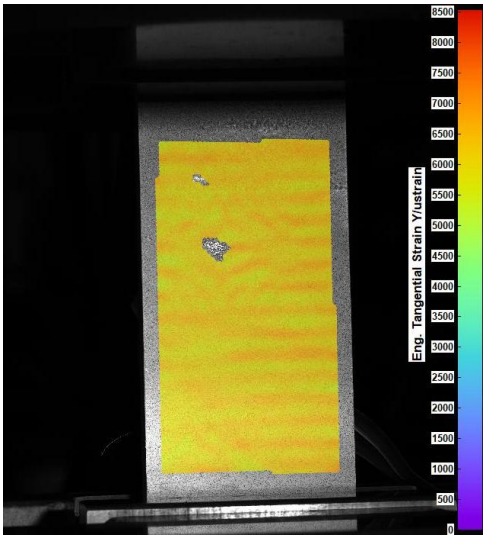
(b) 210KN



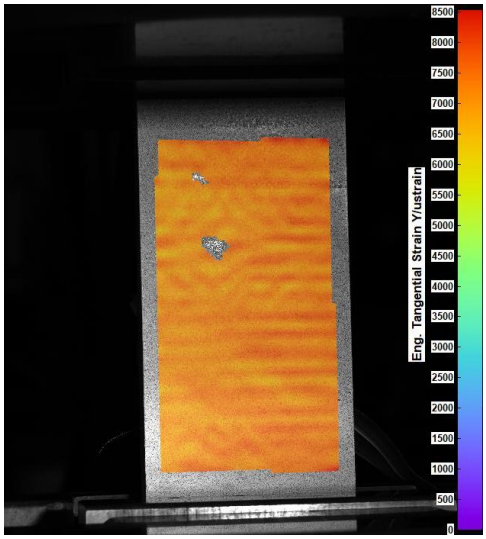
(c) 300KN



(d) 390KN



(e) 510KN



(f) 600KN

Fig. 12. Evolution of the longitudinal surface strain field obtained via DIC at various load levels

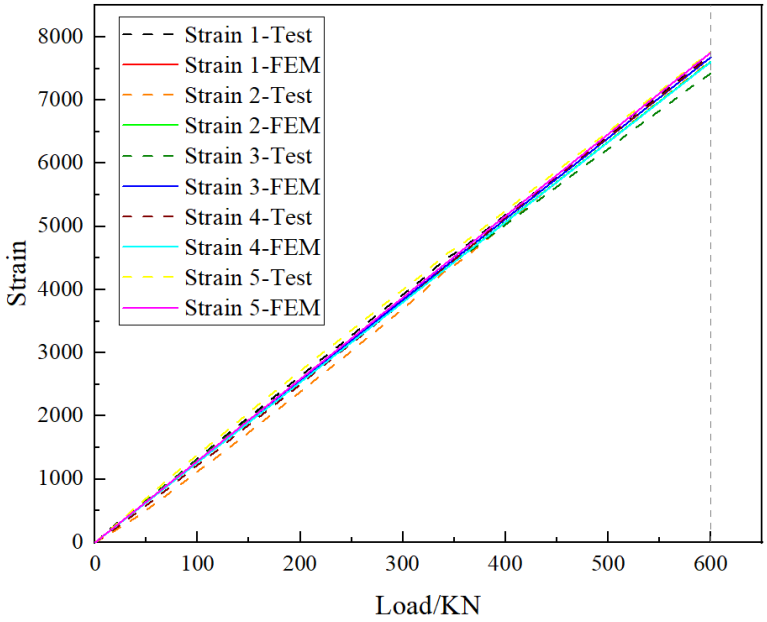


Fig. 13. Comparison of the experimental and numerical load-strain curves throughout the entire loading history (RS7-WLS-1)

Table 5. Comparison of the maximum longitudinal strains between experimental measurements and FEM predictions at a target tensile load of 600 kN

	Number	RS7-LS-1	RS7-LS-2	RS7-LS-3	RS7-LS-4	RS7-LS-5	RS7-LS-6	Average	FEM	Error/%
Maximum longitudinal strain (%)	Strain 1	7407	7366	7998	7774	7714	8077	7722.67	7753	0.39
	Strain 2	7514	7611	7759	7622	7439	7914	7643.17	7612	0.41
	Strain 3	7384	7858	7892	7679	7435	7753	7666.83	7680	0.17
	Strain 4	7334	7883	7709	7832	7745	8017	7753.33	7624	1.67
	Strain 5	7526	7658	7658	7749	7764	7735	7681.67	7689	0.10

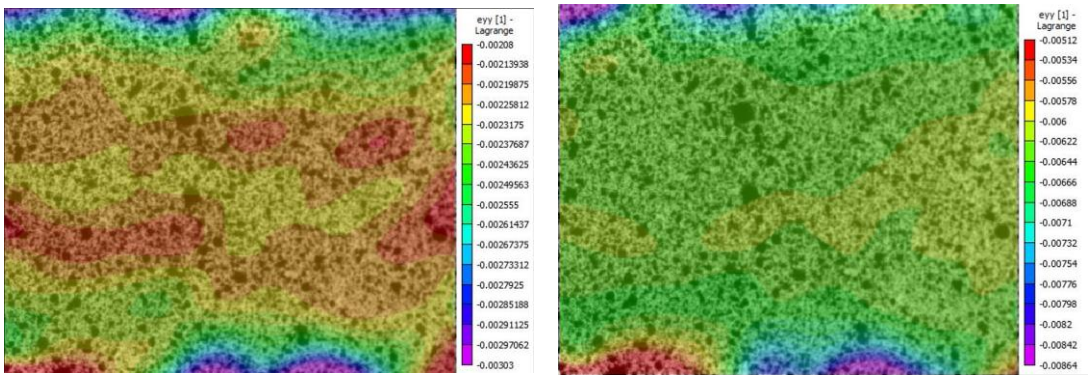
6.1.2 Compressive response and validation of macroscopic stiffness

To further validate the applicability of the proposed 3D equivalent elastic constant model under macroscopic compressive loading, a comparative analysis between uniaxial compression tests and numerical simulations was conducted on the thick-section laminates. Fig. 14 illustrates the evolution of the longitudinal surface strain field for a representative specimen (RS7-YS-1) at three typical load steps: 50 kN, 150 kN, and 250 kN. The full-field strain distributions acquired via DIC indicate that, as the compressive load escalates, the overall strain within the effective gauge section remains highly uniform. In some specimens, slight localized strain fluctuations emerged at the higher load level (250 kN). This phenomenon can likely be attributed to inherent manufacturing features within the thick composite (e.g., resin-rich pockets or micro-voids), which induce localized micro-buckling or non-uniform out-of-plane Poisson's expansion under 3D compressive stress states.

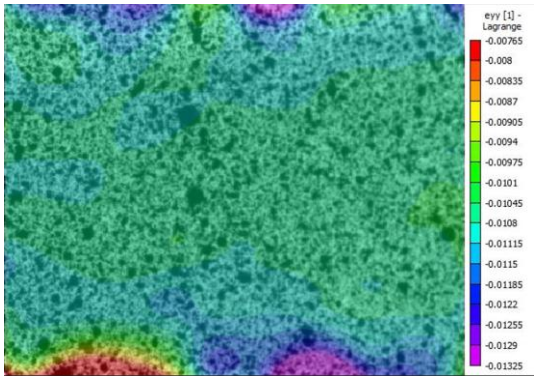
To quantitatively evaluate the predictive accuracy of the equivalent model throughout the entire loading history, the experimental load-strain responses at the in-plane center (Strain 2) and lateral center (Strain 1) were extracted and compared with the corresponding FEM predictions (Fig. 15 and Fig. 16). The experimental curves demonstrate that for all six replicate specimens, the load-strain trajectories—on both the in-plane and lateral surfaces—exhibit pronounced linearity and minimal scatter from the initial loading phase up to imminent ultimate failure. This not only reflects the excellent manufacturing stability of the thick laminates but also mechanistically confirms the

absence of macroscopic Euler buckling instability during uniaxial compression; the macroscopic deformation is entirely governed by the material's intrinsic compressive stiffness. The comparative results clearly reveal that the slopes of the FEM-predicted load-strain curves are in excellent agreement with the experimental curve clusters in both in-plane and lateral directions. Given that the slope of a load-strain curve directly represents the macroscopic structural stiffness, this high-fidelity correlation over the entire history powerfully substantiates that the derived 3D equivalent elastic constants can accurately characterize the macroscopic linear-elastic constitutive behavior of thick laminates under 3D compressive stress states.

Furthermore, Table 6 presents a quantitative comparison between the average maximum longitudinal strains measured experimentally and the FEM nodal predictions. The results indicate that at the two lateral locations (Strain 1 and Strain 3), the FEM predictions (1.076% and 1.075%) closely match the experimental averages (1.038% and 1.043%), yielding relative errors of merely 3.66% and 3.07%, respectively. For the in-plane central location (Strain 2), the average experimental strain is 1.07% against an FEM prediction of 1.140%, resulting in a relative error of 6.54%. Overall, the localized strain prediction on the lateral surfaces is slightly superior to that on the in-plane surface. This discrepancy primarily arises because thick plates subjected to extreme uniaxial compression experience slight out-of-plane nonlinear dilatational deformation. Consequently, the equivalent model, premised on homogenization assumptions, possesses inherent theoretical limitations in capturing localized nonlinear geometric distortions on the surface. Nevertheless, the relative errors across all measurement points are strictly constrained within 7%, comprehensively demonstrating that the macroscopic finite element model based on 3D equivalent elastic constants can accurately and reliably predict the macroscopic compressive stiffness and global deformation response of thick-section woven laminates.



(a) 50KN (b) 150KN



(c) 250KN

Fig. 14. Evolution of the longitudinal surface strain contour maps acquired via DIC (RS7-YS-1)

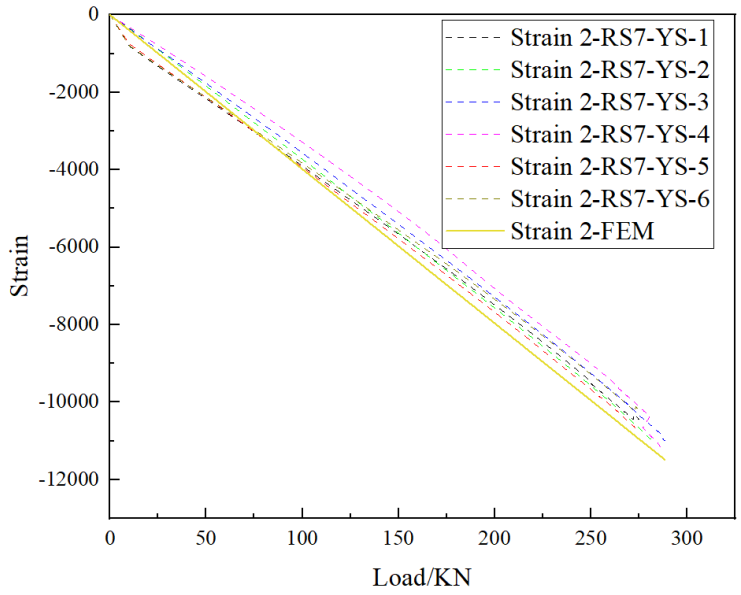


Fig. 15. Comparison of the experimental and numerical in-plane load-strain curves (Strain 2)

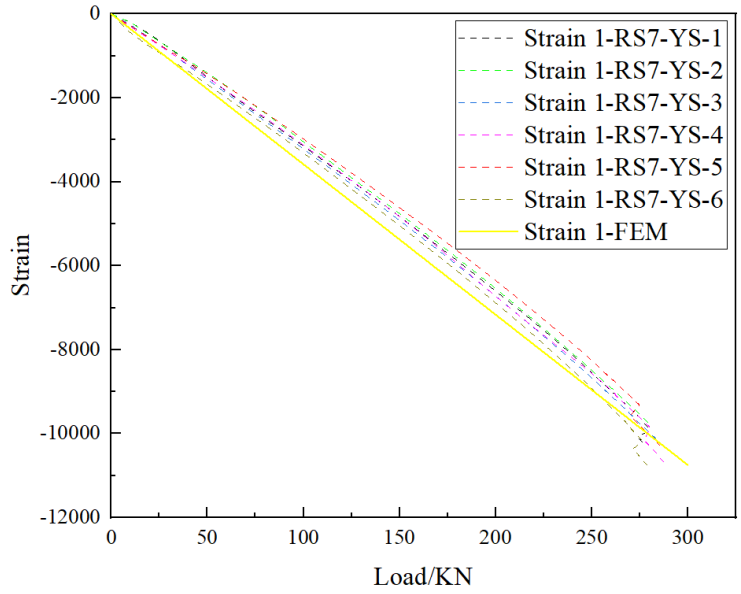


Fig. 16. Comparison of the experimental and numerical lateral load-strain curves (Strain 1)

Table 6. Comparison of the maximum longitudinal compressive strains between experimental measurements and FEM predictions

	Number	RS7-YS-1	RS7-YS-2	RS7-YS-3	RS7-YS-4	RS7-YS-5	RS7-YS-6	Average	FEM	Error/%
Maximum longitudinal strains (%)	Strain 2	1.07	1.10	1.05	1.10	1.02	1.07	1.07	1.140	6.54
	Strain 1	1.08	1.07	1.04	1.03	0.98	1.03	1.038	1.076	3.66
	Strain 3	1.10	1.05	0.97	1.01	1.08	1.05	1.043	1.075	3.07

6.2 Progressive Damage Analysis and Failure Load Prediction

6.2.1 Macroscopic Failure Morphology

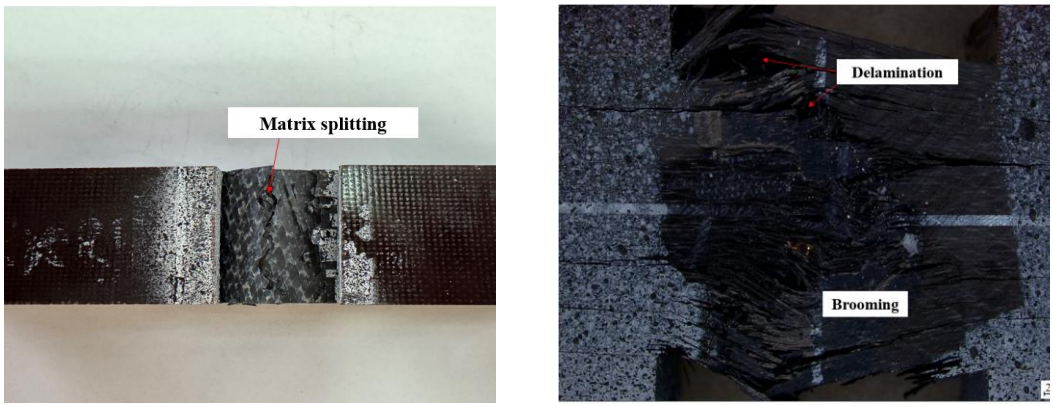
During the initial phase of uniaxial compressive loading, the load-displacement response exhibits transient nonlinearity, primarily attributed to the closure of initial gaps between the testing machine fixtures and the specimen's loading surfaces, alongside general system slack accommodation (fixture seating). Subsequently, the structure transitions into a stable linear-elastic response regime, characterized by a constant macroscopic compressive stiffness. Once the applied load reaches the ultimate load-bearing capacity, a loud acoustic emission is detected, accompanied by an instantaneous and severe load drop, culminating in the sudden catastrophic failure of the specimen.

To profoundly elucidate the compressive failure mechanisms of the thick-section laminates, high-resolution morphological observations of the fractured specimens were conducted utilizing a Leica DVM6A digital microscope (Fig. 17), with the results depicted in Fig. 18(a) and 18(b). The macroscopic and microscopic observations reveal that the specimens experienced a typical and severe "brooming" failure mode. From the micrographs, it is unequivocally identifiable that this catastrophic failure is synergistically driven by severe delamination, matrix splitting, and out-of-plane fiber kinking. Given the complex three-dimensional stress states inherent in thick-section laminates, damage cracks typically initiate at the free edges due to acute stress concentrations and rapidly propagate inward, severely weakening the interlaminar interfaces. The onset of localized delamination deprives the load-bearing fibers of their lateral matrix support. Consequently, these unsupported fibers undergo localized instability and kinking under the extreme axial compressive stress. This kinking process is accompanied by intense localized shear dissipation, ultimately resulting in the splayed, broom-like fracture at the specimen's extremities.

Fig. 19 illustrates the simulated failure mode and damage distribution of the specimen at the ultimate load state, predicted by the 3D progressive damage model. Within the VUMAT subroutine, the state variable SDV19 is explicitly designated to represent the fiber compression damage variable. When SDV19 reaches a value of 1.0, it signifies the complete loss of fiber compressive load-bearing capacity at that specific integration point. The simulation results vividly demonstrate that the fiber compressive damage bands exhibit highly localized characteristics through the thickness, evolving along an inclined trajectory akin to a shear band. This numerically predicted damage propagation path exhibits remarkable geometrical correlation with the out-of-plane kink band angle and macroscopic fracture locations observed experimentally in Fig. 18(b). This alignment indicates that the numerical model successfully captures the core physical mechanism: interlaminar failure inducing the loss of lateral support, which subsequently precipitates the catastrophic loss of fiber compressive capacity. Comprehensive comparisons corroborate that the proposed 3D progressive damage analysis framework—integrating the Puck criterion and cohesive zone modeling—not only predicts the ultimate load-bearing capacity of thick laminates with high precision but also authentically replicates the complex, coupled failure mechanisms of fiber kinking and delamination unique to thick-section composites.



Fig. 17. Experimental setup of the Leica DVM6A digital microscope



(a) Distinct matrix splitting

(b) Typical delamination and brooming morphology

Fig. 18. Macroscopic and microscopic failure modes of the compressive specimen

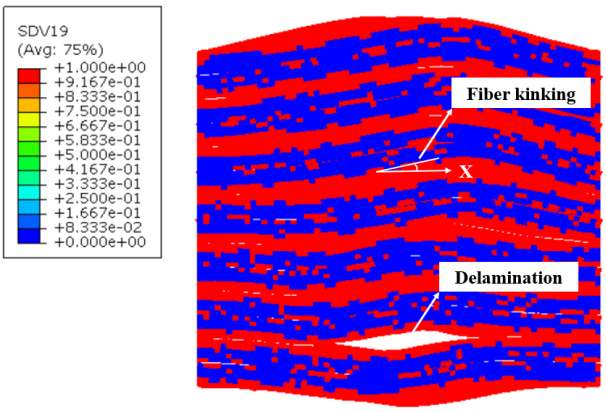


Fig. 19. Simulated failure mode and damage distribution at the ultimate load state

6.2.2 Failure Load Prediction

In accordance with the ASTM D6641 standard [29], the ultimate compressive strength of the unnotched composite laminates is calculated using Eq. (30):

$$F^{\mathrm{cu}} = \frac{P_{\mathrm{f}}}{wh} \tag{30}$$

where F^{cu} denotes the ultimate compressive strength of the laminate (MPa); P_{f} represents the ultimate failure load prior to catastrophic fracture (N); w and h are the width and thickness of the effective gauge section (mm), respectively. Table 7 presents a detailed quantitative comparison between the experimental data obtained from the six replicate compressive specimens and the numerical predictions derived from the 3D progressive damage FEM.

As summarized in Table 7, the average ultimate failure load across the six experimental specimens is 282,733 N, corresponding to an average ultimate compressive strength of 577.01 MPa. In comparison, the FEM predicts an ultimate failure load of 268,100 N, yielding a predicted compressive strength of 569.94 MPa. A comparative analysis clearly reveals that the relative error between the simulated ultimate strength and the experimental average is exceptionally low, standing at a mere 1.23%. This remarkably high predictive fidelity rigorously validates that the proposed 3D progressive damage framework—which deeply integrates the intralaminar Puck failure criterion with the interlaminar cohesive zone model—can acutely capture the complex damage evolution mechanisms and precisely determine the ultimate load-bearing capacity of thick-section composites under severe 3D compressive stress states.

Table 7. Comparison of the ultimate load-bearing capacity and compressive strength between experimental measurements and FEM predictions for the thick-section laminates

Number	P_f /N	Average value/N	FEM/N	F^{cu} /MPa	Average value/MPa	FEM/MPa	Error/%
RS7-YS-1	279987	282733	268100	565.63	577.01	569.94	1.23
RS7-YS-2	281240			568.16			
RS7-YS-3	289681			585.21			
RS7-YS-4	280649			566.97			
RS7-YS-5	285252			576.27			
RS7-YS-6	279587			564.82			

7. Conclusion

This study systematically investigated the 3D equivalent elastic response and progressive failure mechanisms of thick-section composite laminates through a synergistic experimental and numerical approach. The main conclusions are presented as follows:

(1) The proposed 3D equivalent elastic constant theory successfully bridges the gap between classical laminate theory and fully discrete 3D models. Validation against full-field DIC measurements confirms that the homogenized sub-laminate model accurately captures the linear-elastic response under both tension and compression, with localized strain errors consistently constrained within 7%. This demonstrates the framework's capability to represent the complex constitutive behavior of thick woven laminates with high computational efficiency.

(2) The developed 3D progressive damage model, which couples the physically-based Puck criterion with a cohesive zone model, not only exhibits exceptional predictive accuracy for ultimate strength—achieving a negligible relative error of 1.23%—but also explicitly clarifies the cascading "brooming" failure sequence. The analysis demonstrates that failure initiates as interlaminar delamination at free edges, which deprives the load-carrying fibers of their lateral matrix support and triggers catastrophic out-of-plane kinking and shear-driven matrix splitting.

(3) By systematically addressing the macroscopic stiffness via the computationally efficient 3D homogenization scheme and the ultimate load-bearing capacity via the high-fidelity progressive damage model, this research establishes a comprehensive and rigorously validated analytical methodology for thick-section composites. This dual-pronged approach effectively accommodates the different requirements of structural analysis—balancing computational cost for stiffness evaluation and physical fidelity for damage localization. Consequently, it provides robust and flexible solutions for the rapid optimization design and airworthiness certification of thick-section primary load-bearing structures in advanced aerospace applications.

References

[1] de Vries H. Development of a main landing gear attachment fitting using composite material and resin transfer moulding. 2009.

[2] Viscardi M, Arena M, Cerreta P, Iaccarino P, Imparato SI. Manufacturing and validation of a novel composite component for aircraft main landing gear bay. J Mater Eng Perform 2019;28(6):3292–300.

[3] Seyednourani, M.; Akgun, S.; Ulus, H.; Yildiz, M.; Sas, H. S. Impact Damage and Low Temperature Effects on Carbon Fiber/Epoxy Joints: A Comparative Study of Hybrid Bolted/Bonded and Bolted Configurations with Cross-Ply and Angle-Ply Laminates. Composites Part A: Applied Science and Manufacturing 2025, 190 (), 108677.

[4] H. Senol, H. Ulus, A. Al-Nadhari, S. Topal, and M. Yildiz. Ameliorating tensile and fracture performance of carbon fiber-epoxy composites via atmospheric plasma activation: Insights into damage modes through in-situ acoustic emission inspection. *Compos. Part Appl. Sci. Manuf.*, vol. 195, p. 108929, Aug. 2025.

[5] A. Al-Nadhari, H. Ulus, S. Topal, and M. Yildiz. Analyzing stiffness variations in 3D woven composites: A multi-instrumental study on Glass/Kevlar hybridization effects under tensile and shear loads. *Compos. Part Appl. Sci. Manuf.*, vol. 191, p. 108722, Apr. 2025.

[6] C. Yildirim, H. Ulus, H. S. Sas, and M. Yildiz. Evaluating the influence of service conditions on the out-of-plane and in-plane loading performance and damage behavior of unidirectional CF/PEKK composites for aerospace applications. *Compos. Part B Eng.*, vol. 304, p. 112637, Sep. 2025.

[7] M. Seyednourani, S. Akgun, H. Ulus, M. Yildiz, and H. S. Sas. Impact damage and low temperature effects on carbon fiber/epoxy joints: A comparative study of hybrid bolted/bonded and bolted configurations with cross-ply and angle-ply laminates. *Compos. Part Appl. Sci. Manuf.*, vol. 190, p. 108677, Mar. 2025.

[8] F. E. Yakin, C. O. Senol, N. Birgün, H. Ulus, M. Yildiz, and H. S. Sas. Influence of stacking sequence and compaction force during the AFP process on mechanical performance and damage mechanisms elucidated by acoustic emission insights. *Proc. Inst. Mech. Eng. Part J. Mater. Des. Appl.*, vol. 240, no. 1, pp. 19–34, Jan. 2026.

[9] M. Toozandehjani. Conventional and Advanced Composites in Aerospace Industry: Technologies Revisited. *Am. J. Aerosp. Eng.*, vol. 5, no. 1, p. 9, 2018.

[10] Besson, J-M., M-A. Celli, and Nicolas Capelle. H160 Helicopter: development of a carbon thermoplastic hub. 2016.

[11] H. Yildiz and M. Sarikanat. Finite-element analysis of thick composite beams and plates. *Compos. Sci. Technol.*, vol. 61, no. 12, pp. 1723–1727, Sep. 2001.

[12] S. Onodera and T. Okabe. Three-dimensional analytical model for effective elastic constants of transversely isotropic plates with multiple cracks: Application to stiffness reduction and steady-state cracking of composite laminates. *Eng. Fract. Mech.*, vol. 219, p. 106595, Oct. 2019.

[13] S. Jangravi, A. Reali, and P. K. Masjedi. Isogeometric analysis for accurate 3D stress recovery of thick laminated composite plates using higher-order shear deformation theory. *Eur. J. Mech. - ASolids*, p. 105935, Oct. 2025.

[14] Y. Jiang, Y. Liu, J. Zeng, Y. Wang, Q. Xie, and N. Hu. Equivalent elastic modulus measurement of cross-ply composite plates using Lamb waves. *Compos. Struct.*, vol. 321, p. 117230, Oct. 2023.

[15] K. Zheng, H. Hu, D. Cao, Y. Zhong, and S. Li. Experimental and numerical studies on the tensile behaviors of thin-ply and thick-ply open-hole laminates. *Thin-Walled Struct.*, vol. 186, p. 110649, May 2023.

[16] A. Ollic, F. Sheibanian, B. Fazlali, Y. Swolfs, S. V. Lomov, and V. Carvelli. Modelling the damage evolution in unidirectional all-carbon hybrid laminates. *Compos. Sci. Technol.*, vol. 247, p. 110420, Mar. 2024.

[17] T. Martinoni, V. Ott, V. Carvelli, and G. P. Terrasi. Tensile behavior of unidirectional thick-Ply all-carbon hybrid laminates: a systematic experimental and numerical study. *Compos. Part C Open Access*, vol. 14, p. 100462, Jul. 2024.

[18] M. S. Loukil *et al.* Experimental and numerical investigation on bearing behavior of hybrid thin/thick-ply composite laminates. *Compos. Struct.*, vol. 331, p. 117888, Mar. 2024.

[19] M. G. Bateman *et al.* Measurement of residual stress in thick section composite laminates using the deep-hole method. *Int. J. Mech. Sci.*, vol. 47, no. 11, pp. 1718–1739, Nov. 2005.

[20] Y. Gao *et al.* Thickness variation effect on compressive properties of ultra-thick CFRP laminates. *Int. J. Mech. Sci.*, vol. 253, p. 108390, Sep. 2023.

[21] Y. Gao *et al.* Investigation on the compressive mechanical properties of ultra-thick CFRP laminates. *Int. J.*

Mech. Sci., vol. 241, p. 107966, Mar. 2023.

[22] J. Lee and C. Soutis. A study on the compressive strength of thick carbon fibre–epoxy laminates. *Compos. Sci. Technol.*, vol. 67, no. 10, pp. 2015–2026, Aug. 2007.

[23] F. Lahuerta, R. P. L. Nijssen, F. P. Van Der Meer, and L. J. Sluys. Thickness scaled compression tests in unidirectional glass fibre reinforced composites in static and fatigue loading. *Compos. Sci. Technol.*, vol. 123, pp. 115–124, Feb. 2016.

[24] N. Van Hoorn, S. Turteltaub, C. Kassapoglou, and W. Van Den Brink. Numerical prediction of impact damage in thick fabric composite laminates. *Compos. Struct.*, vol. 353, p. 118726, Jan. 2025.

[25] M. Spencer and X. Chen. Static and fatigue cracking of thick carbon/glass hybrid composite laminates with complex wrinkle defects. *Int. J. Fatigue*, vol. 177, p. 107963, Dec. 2023.

[26] S. Rai and B. P. Patel. A failure mode dependent continuum damage model for thick laminated composite plates. *Mech. Mater.*, vol. 186, p. 104790, Nov. 2023.

[27] Y. Chen, X. Liang, B. Wang, and H. Shi. An experimental investigation of the compressive failure in quasi-isotropic ultra-thick CFRP laminates. *Compos. Struct.*, vol. 354, p. 118818, Jan. 2025.

[28] ASTM D3039/D3039M – 17 Standard Test Method for Tensile Properties of Polymer Matrix Composite Materials, ASTM International, West Conshohocken, PA, 2017.

[29] ASTM D6641/D6641M – 23 Standard Test Method for Compressive Properties of Polymer Matrix Composite Materials Using a Combined Loading Compression (CLC) Test Fixture, ASTM International, West Conshohocken, PA, 2023.

[30] C. T. Sun and Sijian Li. Three-Dimensional Effective Elastic Constants for Thick Laminates. *J. Compos. Mater.*, vol. 22, no. 7, pp. 629–639, Jul. 1988.

[31] J. Zhi and T.-E. Tay. Interrogating failure mechanisms of notched composites through a discrete crack modeling approach. *Compos. Sci. Technol.*, vol. 196, p. 108203, Aug. 2020.

[32] S. Pimenta, R. Gutkin, S. T. Pinho, and P. Robinson. A micromechanical model for kink-band formation: Part I — Experimental study and numerical modelling. *Compos. Sci. Technol.*, vol. 69, no. 7–8, pp. 948–955, Jun. 2009.

[33] O. Hoffman. The Brittle Strength of Orthotropic Materials. *J. Compos. Mater.*, vol. 1, no. 2, pp. 200–206, Apr. 1967.

[34] Toyoda, M. Strength characteristics of composite materials. Welding International, 5(5), 341–345. 1991.

[35] Hashi, Z. J. J. O. A. M. Failure criteria for unidirectional fiber composite. Journal of Applied Mechanics, 47, 3292334. 1980.

[36] Hashin, Z. Fatigue Failure Criteria for Unidirectional Fiber Composites. ASME. J. Appl. Mech. December 1981; 48(4): 846–852.

[37] Chang K-Y, Llu S, Chang F-K. Damage Tolerance of Laminated Composites Containing an Open Hole and Subjected to Tensile Loadings. Journal of Composite Materials. 1991;25(3):274-301.

[38] Chang F-K, Chang K-Y. A Progressive Damage Model for Laminated Composites Containing Stress Concentrations. Journal of Composite Materials. 1987;21(9):834-855.

[39] A. Puck and H. Schürmann. Failure analysis of FRP laminates by means of physically based phenomenological models.

[40] L. Zhao, Y. Gong, J. Zhang, Y. Chen, and B. Fei. Simulation of delamination growth in multidirectional laminates under mode I and mixed mode I/II loadings using cohesive elements. *Compos. Struct.*, vol. 116, pp. 509–522, Sep. 2014.

[41] L. Zhao, J. Zhi, J. Zhang, Z. Liu, and N. Hu. XFEM simulation of delamination in composite laminates. *Compos. Part Appl. Sci. Manuf.*, vol. 80, pp. 61–71, Jan. 2016.

[42] Dassault Systemes Simulia Corp, Abaqus User's Manual, 2016.

[43] G. Zhang, M. Tong, B. Yan, and S. Zhu. Compression-After-Impact Performance of CFRP Laminates With Pre-Embedded Delamination Subjected to Low-Velocity Impact and Bolted Reinforcement. *Polym. Compos.*, vol. 47, no. 1, pp. 319–335, Jan. 2026.